On the Definition of an Independent Stochastic Model for InSAR Time Series

Wietske S. Brouwer and Ramon F. Hanssen, *Senior Member, IEEE*

***Abstract*—InSAR enables the estimation of displacements of (objects on) the Earth's surface. To provide reliable estimates, both an independent stochastic and functional model are required. However, the intrinsic problem of InSAR is that both are unknown. Here we propose an independent definition of the stochastic model, via an approximation scheme for the variance-covariance matrix for double-differenced phase observations for an arc, i.e., the phase difference between two points relative to a reference epoch. Detecting temporal partitions in the amplitude time series, we assign quality values to all phase observations within each partition. To reduce the impact of outliers, we introduce the Normalized Median Absolute Deviation (NMAD) of the vector of amplitudes to robustly estimate the variance of the phase observations. The method results in a scatterer-specific and time-variable stochastic model, which is independent of the phase observations itself and prior to parameter estimation. This differs from many conventional methods where the quality is often determined a posteriori from the residuals between the model and the observations. This yields more realistic and reliable displacement estimates, as well as improved statements on the precision and reliability of the estimated parameters.**

***Index Terms*—InSAR, surface displacements, stochastic model, parameter estimation**

I. Introduction

InSAR (SAR Interferometry) is a geodetic technique that enables the estimation of the displacement of (objects on) the Earth's surface. Even though the results are often visualized as displacements of a set of (point or distributed) scatterers, in fact they should be interpreted as the motion of an arc, formed by two scatterers. The original observation corresponding to this arc is the double-differenced (DD) phase, i.e., the phase difference between a scatterer and a reference scatterer, relative to a reference epoch [1]. To estimate displacement parameters from this DD phase observation, both a proper functional and stochastic model are required [2], where the functional model describes the relation between the observables and the unknown parameters, and the stochastic model describes the uncertainty or variability of the data [3]. However, the fundamental problem of InSAR is that both models are unknown and different for each scatterer and even epoch. For example using Point Scatterers (PS) [4], [5], it is generally not known exactly from which (part of an) object the main signal originates, resulting in an unknown kinematic behavior, which should be expressed in the functional model. This problem is especially important in the built environment [6]. Regarding the stochastic model, the quality of a phase observation at a single epoch is intrinsically unknown, and each scatterer will have unique scattering properties, which may change over time [5], [7]. In conventional PSI methodologies the quality of the observations is often only calculated in hindsight, based on the residuals between the observations and the model evaluated from the estimates [8], [9], which introduces an intricate and unacceptable dependency on the correctness of the functional model [10], [11], [12]. Consequently, for arcs with a complex displacement behavior, the unmodeled displacements are typically interpreted as noise, and a posteriori assigned to the stochastic model, resulting in an underestimation of the quality, or even the outright rejection of the scatterer.

The stochastic model should be known before, and independently of, the parameter estimation. An independent first-order approximation of the stochastic model would enable us to weigh points relative to each other and to make a better selection of which points (or arcs) are going to be evaluated. Moreover, it is indispensable for testing the entire mathematical model [9]. A stochastic model that is chosen too conservatively may lead to sustaining the null hypothesis (e.g., of steady-state motion) while it should be rejected.

Yet, approximating the variance-covariance matrix of the DD phase observation for each arc, independent of the phase observations themselves, is complex. Here we split this problem into several steps. First, we demonstrate that the variance-covariance matrix (VCM) of the DD phases can be derived from the VCM of the single-look complex (SLC) phases. While deriving temporal phase differences may seem straightforward at first glance, various methodological choices yield distinct results, in particular related to the treatment of the reference acquisition. This is discussed in Sec. III. Secondly, the VCM of the DD phase observations contains several contributing components: atmospheric noise, time variant clutter (TVC), and thermal noise. In Sec. IV, we discuss these three components in more detail and how the VCM for each component should be derived. Building upon the approach proposed by Ferretti et al. [4], we exploit the amplitude data to estimate the phase dispersion. To account for a varying phase quality over time, we then use the amplitude time series to detect partitions and then estimate the quality for the phase data for each partition. We introduce the concept of the Normalized Median Absolute Deviation (NMAD) instead of the widely used Normalized Amplitude Dispersion (NAD) to approximate the phase quality and be less sensitive for outliers.

W.S. Brouwer and R.F. Hanssen are with the Department of Geoscience and Remote Sensing, Delft University of Technology, Delft, 2628 CN, The Netherlands (email: w.s.brouwer@tudelft.nl, r.f.hanssen@tudelft.nl).

II. The mathematical model

After the selection of potentially coherent point scatterers[1], the temporal single difference phase ϕ_j^{md} for point scatterer j is the SLC phase, denoted by $\{\psi \mid -\pi \leq \psi < \pi, \psi \in \mathbb{R}\}$, of daughter[2] image d relative to the phase of the mother image m, i.e., $\underline{\phi}_j^{md} = \underline{\psi}_j^{d} - \psi_j^{m}$, with $\{\phi \mid -\pi \leq \phi < \pi, \phi \in \mathbb{R}\}$, is computed using complex multiplication [1]. The underline expresses the stochastic nature of the observables, where the mother image is considered to be deterministic, see section III-A. Since a temporal difference of one point is meaningless, the spatial difference between this point j and a reference point i needs to be considered. Via complex multiplication this yields a spatio-temporal double difference (DD) phase φ_{ij}^{md}, with $\{\varphi \mid -\pi \leq \varphi < \pi, \varphi \in \mathbb{R}\}$, which represents the phase for point scatterer j at epoch d, relative to reference point i at mother epoch m. The DD phase is the sum of different components:

$$\begin{aligned}\underline{\varphi}_{ij}^{md} =& \underline{\phi}_j^{md} - \underline{\phi}_i^{md} \\ =& -2\pi a_{ij}^{md} + \varphi_{ij,D}^{md} + \varphi_{ij,H}^{md} + \underline{\varphi}_{ij,S}^{md} + \underline{\varphi}_{ij,n}^{md},\end{aligned} \tag{1}$$

where $a \in \mathbb{Z}$ is the integer ambiguity, φ_D the displacement phase, and φ_H, φ_S, and φ_n the phases due to the residual cross-range distance H, the superposed atmospheric phase screens from epoch m and d, and noise, respectively. The main signals of interest are the residual cross-range distance and the displacement phase. The mathematical model (for the absolute phase) therefore becomes

$$E\{\begin{bmatrix}\underline{\varphi}_{ij}^{md_1} \\ \vdots \\ \underline{\varphi}_{ij}^{mD}\end{bmatrix}\} = \underbrace{(D_A|B_T) + (\mu_{\Delta T} L_{\text{LoS}}|B_{\text{th}})}_{\varphi_{ij,D}^{md}} + \underbrace{(H_{ij}|B_\perp)}_{\varphi_{ij,H}^{md}}; \tag{2}$$

$$\underbrace{D\{\begin{bmatrix}\underline{\varphi}_{ij}^{md_1} \\ \vdots \\ \underline{\varphi}_{ij}^{mD}\end{bmatrix}\}}_{\underline{y}} = Q_{\varphi_{ij}} = \underbrace{Q_{\varphi_{ij},\text{atm}}}_{\varphi_{ij,S}^{md}} + \underbrace{Q_{\varphi_{ij},\text{TVC}} + Q_{\varphi_{ij},\text{thn}}}_{\varphi_{ij,n}^{md}}, \tag{3}$$

where $E\{.\}$ is the expectation operator, and the vector of unknown parameters contains D_A: the relative non-thermal displacement (as a function of the temporal baseline B_T); $\mu_{\Delta T} L_{\text{LoS}}$: the relative thermal displacement (as a function of thermal baseline B_{th}), and residual cross-range distance H_{ij} (as a function of perpendicular baseline $B_\perp$). $D\{.\}$ describes the dispersion of the observations described by the Variance Covariance Matrix (VCM), $Q_{\varphi_{ij}}$, which is the sum of (i) the atmospheric noise, $Q_{\varphi_{ij},\text{atm}}$, (ii) the thermal noise, $Q_{\varphi_{ij},\text{thn}}$, and (iii) the Time Variant Clutter (TVC) $Q_{\varphi_{ij},\text{TVC}}$. In the following, we will show that by using error propagation, the VCM of the DD phases can be derived once the VCM of the SLC phases, Q_ψ, is known.

[1]In this study, we use the term "point" to refer to either a Point Scatterer or a Distributed Scatterer.

[2]We refer to 'mother and daughters,' where the mother image is defined as the reference image.

III. Derivation of the VCM for an arc

The vector of SLC phase observations for point scatterer i is defined as

$$\underline{\psi}_i = [\underline{\psi}_i^m, \underline{\psi}_i^{d_1}, \underline{\psi}_i^{d_2}, \ldots, \underline{\psi}_i^{d_D}]^T. \tag{4}$$

For convenience the first image is defined as the mother image, but this is arbitrary. The VCM of the observations is

$$Q_{\psi_i} = \begin{bmatrix}\sigma^2_{\psi_i^m} & 0 & \ldots & 0 \\ 0 & \sigma^2_{\psi_i^{d_1}} & & \vdots \\ \vdots & & \ddots & \\ 0 & \ldots & & \sigma^2_{\psi_i^{d_D}}\end{bmatrix}, \tag{5}$$

where the different SLC observations are considered to be uncorrelated [13]. Since this SLC phase is meaningless, double differences, both in time and in space, need to be formed [1]. In the following we first discuss how the temporal single phase differences should be computed, followed by the computation of the spatial differences.

A. Computing the single differences (in time)

The temporal phase differences, here referred to as Single Differences (SD), ϕ_i, and the corresponding VCM, Q_{ϕ_i}, can be computed following three possible approaches that differ primarily in whether the mother image is treated as a deterministic quantity or a stochastic variable. We simulated SLC values[3] for one mother and five daughters[4] to demonstrate the effect of the three different approaches, see Fig. 1. The

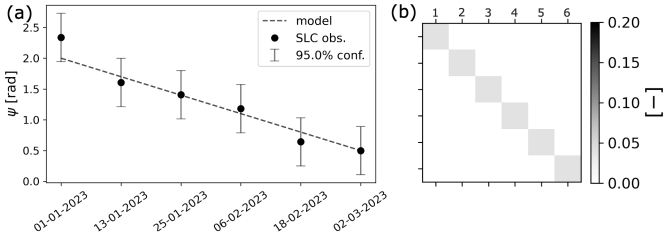

Fig. 1: (a): simulated SLC phase observations for point i with a particular trend shown by the dashed line. (b) variance-covariance matrix of the SLC phase observations: all observations have the same quality and the observations are uncorrelated.

representation of the SLC phase observations in Fig. 1a is defined as a '*position graph*', i.e., the phases are measured at a particular epoch, and the vertical axis shows the 'position' (in this case the observed phase) at a particular epoch. The horizontal axis therefore expresses time as a date. Below, we discuss the three subsequent possibilities to treat the mother acquisition.

[3]Note that in reality there cannot be a trend in the SLC observations, since the phase distribution is a uniform distribution between $-\pi$ and π based on the scattering mechanism only. Yet, we simulate SLC observations with a trend to highlight the consequences of the different approaches.

[4]Obviously current InSAR time series may contain hundreds of epochs, the small number of acquisitions helps in highlighting this differences between the three methods

1) Approach 1: Disregarding the temporal phase difference of the mother with itself, a.k.a. 'eliminating mother': Perhaps the most conventional approach for computing the SD values is by using the differencing matrix,

$$\underbrace{\begin{bmatrix} \underline{\phi}_i^{md_1} \\ \underline{\phi}_i^{md_2} \\ \underline{\phi}_i^{md_3} \\ \vdots \\ \underline{\phi}_i^{md_D} \end{bmatrix}}_{\underline{\phi}_i} = \underbrace{\begin{bmatrix} -1 & 1 & 0 & \cdots & 0 \\ -1 & 0 & 1 & \cdots & 0 \\ \vdots & \vdots & \vdots & \ddots & \vdots \\ -1 & 0 & 0 & \cdots & 1 \end{bmatrix}}_{A} \underbrace{\begin{bmatrix} \underline{\psi}_i^{m} \\ \underline{\psi}_i^{d_1} \\ \underline{\psi}_i^{d_2} \\ \vdots \\ \underline{\psi}_i^{d_D} \end{bmatrix}}_{\underline{\psi}_i}, \tag{6}$$

where D is the number of daughter acquisitions, as in [4], [14], [8]. Using error propagation the stochastic model for the SD phase values is computed with

$$Q_{\phi_i} = A Q_{\psi_i} A^T, \tag{7}$$

which will be a full matrix. Fig. 2a shows the consequence of this approach, plotting the SD together with an error bar which represents the 95% confidence interval obtained from the diagonal of Q_{ϕ_i}. The most obvious consequence of this approach is that only D SD phase values are derived from $D+1$ SLC phase values, since the mother epoch is eliminated in the differencing operation. Consequently, plotting the obtained SD phases against absolute (calendar) dates on the horizontal axis, similar to Fig. 1, is no longer possible, indicated by the crossed-out dates. Each phase difference corresponds to a specific time *difference* rather than a time. In contrast to the *position graph* of Fig. 1, this type of graph is referred to as a '*displacement graph*.'

The modeled (simulated) trend, used as ground truth for comparison, is shown by the black dashed line. Subsequently, we estimate a trend and an offset through the obtained single differences, shown by the black solid line. The estimated trend is very similar to the simulated trend. However, comparing the 95% confidence bars of the SD phases (Fig. 2a) with the confidence bars of the SLC phases (Fig. 1), we observe that the confidence bars of the SD phases are larger, i.e., lower precision. This can also be observed comparing the VCM of the SD phases (Fig. 2d) with the VCM of the SLC phases (Fig. 1b). This is a direct result of the definition of the differencing approach, where the stochastic SLC phase vector, $\underline{\psi}_i$, has a particular precision for each single observation. The precision of the derived SD phase is straightforwardly $\sigma^2_{\phi_i^{md}} = \sigma^2_{\psi_i^m} + \sigma^2_{\psi_i^d}$., i.e., the variance of ϕ_i^{md} is the sum of the SLC phase variances of the mother and the daughter acquisition. Since the VCM shown in Fig. 2d becomes a full matrix the complete VCM is required when estimating displacement parameters. Using only the diagonal elements of the VCM to describe the quality of the SD phases results in a too conservative quality estimation for the displacement parameters, and the error bars in Fig. 2a are not sufficient to visualize the quality of the result. The gray zones in Figs. 2a–c are positioned around the adjusted observations and indicate the 95% confidence region of these adjusted observations.

Finally, acknowledging that Fig. 2a is a displacement graph rather than a position graph implies that the interpretation of a point in the graph at time $dt = t - t_m$ is 'the displacement estimated between t and t_m,' where t_m is the absolute date of the mother acquisition. Note that due to the differencing operation the obtained result becomes irreversible.

2) Approach 2: A deterministic temporal phase difference with the mother, a.k.a. 'fixing mother': One possibility to use a position plot with absolute dates, rather than a displacement plot, is to include the SD phase value of the mother with itself in the SD phase vector, i.e., $\phi_i^{mm} = \psi_i^m - \psi_i^m = 0$ resulting in:

$$\underline{\phi}_i = [\phi_i^{mm}, \underline{\phi}_i^{md_1}, \underline{\phi}_i^{md_2}, \underline{\phi}_i^{md_3}, \ldots, \underline{\phi}_i^{md_D}]^T, \tag{8}$$

where $\phi_i^{mm} = 0$ by definition. Note that ϕ_i^{mm} is deterministic, i.e., in Fig. 2b it does not have an error bar. Therefore, we introduce a row and column of zeros in the stochastic model, as depicted in the VCM in Fig. 2e. Utilizing this VCM we can again estimate a model through the SD phases, represented by the solid black line in Fig. 2b. As ϕ_i^{mm} is deterministic, the estimated model is constrained to pass through that value. Upon comparing the estimated model with the true simulated model (the dashed line) and the model estimated with the first approach (the dash-dotted line), it is evident that the estimated average velocity differs substantially from the simulated value. In fact, the trend is significantly biased by adding the deterministic SD of the mother with itself. While this bias may effectively decrease when the time series includes more epochs, this example proves that the 'fixing mother' approach is incorrect. The gray zone in Fig. 2b is positioned around the adjusted observations and indicates their 95% confidence region. This also erroneously suggests that the quality of the adjusted observations temporally closer to the mother are better.

As both approach 1 and approach 2 prove to be fundamentally flawed, the mother acquisition has to be treated differently, as discussed below.

3) Approach 3: Subtracting mother realization from variates, a.k.a. 'embracing mother': The third and preferred approach to compute the SD phase values is by differencing the stochastic variates of all epochs with the deterministic realization of the mother epoch, i.e.,

$$\underbrace{\begin{bmatrix} \underline{\phi}_i^{mm} \\ \underline{\phi}_i^{md_1} \\ \underline{\phi}_i^{md_2} \\ \vdots \\ \underline{\phi}_i^{md_D} \end{bmatrix}}_{\underline{\phi}_i} = \underbrace{\begin{bmatrix} \underline{\psi}_i^{m} \\ \underline{\psi}_i^{d_1} \\ \underline{\psi}_i^{d_2} \\ \vdots \\ \underline{\psi}_i^{d_D} \end{bmatrix}}_{\underline{\psi}_i} - \psi_i^m. \tag{9}$$

This way, with $D+1$ SLC phases, we retain $D+1$ single difference phase values since the SD phase for the mother variate, $\underline{\psi}_i$, relative to its realization ψ_i is computed as well.

Fig. 2c is the corresponding graphical representation, i.e., a position graph. In comparison with Figs. 2a and b, it is clear that adding the mother image appreciates and visualizes all epochs including the reference one. However, even though the single-difference phase value of the mother epoch is equal to zero, it is now stochastic, similar to all other epochs. The estimated average velocity (the solid line) is parallel to the

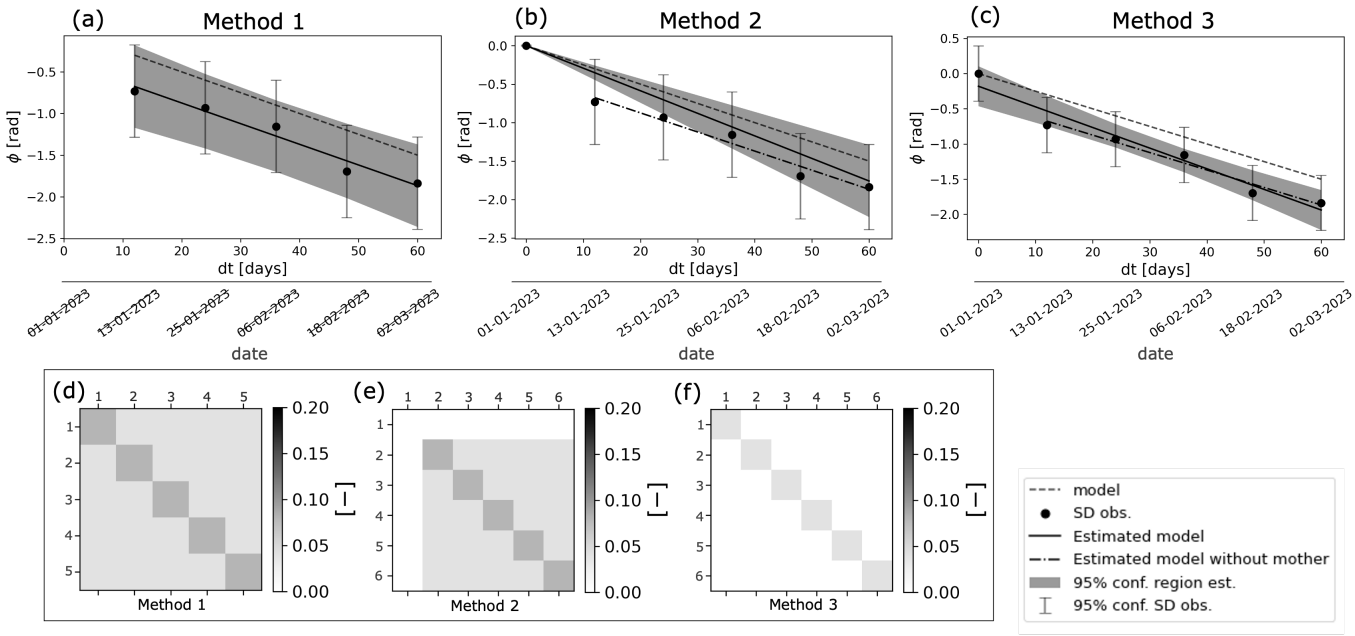

Fig. 2: In (a), (b), and (c) we show the single difference phase values resulting from the three different approaches to compute the SD phase values. In (d), (e), and (f) the obtained variance-covariance matrices (VCM) are shown. In (a) we obtain five SD phase values, i.e., the temporal phase difference at the mother epoch is missing. Therefore the SD phases should be plotted with the delta time at the horizontal axis. In (b) the temporal phase difference at the mother epoch is added as a deterministic value, resulting in the fact that the estimated displacement model passes trough this value, resulting in an erroneous estimated model (the solid black line's slope differs from the simulated velocity shown by the dashed line). In (c) six SD phase values are obtained all being stochastic and resulting in the correct estimated velocity.

simulated (true) average velocity, and it is not forced to pass precisely trough the temporal phase at the mother epoch. The gray zone in Fig. 2c is a correct representation of the quality of the adjusted observations, and indicates the 95% confidence region of these adjusted observations.

The most important consequence of this approach is that the distribution of the single-difference phase differences, represented by $\underline{\phi}_i$, is equivalent to that of the original SLC phases $\underline{\psi}_i$, i.e., $Q_{\phi_i} = Q_{\psi_i}$. This equivalence is trivial, as subtracting a deterministic value from a vector of stochastic variates should not alter the distribution of the resultant derived variate. As a practical consequence, the equivalence implies that the VCM of the single-difference vector remains a diagonal matrix, which is advantageous from a computational and visualization perspective.

Fig. 3 presents the subsequent building blocks to establish the stochastic model for a vector of derived double-difference observations for an arc between point i and j with 11 epochs, i.e., $Q_{\varphi_{ij}}$. The first column, "SLC", describes the Q_ψ matrices of the SLC phases for both points, regarding the clutter and the atmospheric contributions. The second column, "IFG", represents the single (temporal) differences Q_ϕ for both points, relative to the mother epoch. This demonstrates the identity between Q_{ϕ_i} and Q_{ψ_i}, and the absence of correlation.

B. Computing the double differences (in space and time)

Given the temporal SD phase values for point i and j, the spatio-temporal DD phases for the arc are computed with

$$\underbrace{\begin{bmatrix} \underline{\varphi}_{ij}^{mm} \\ \underline{\varphi}_{ij}^{md_1} \\ \underline{\varphi}_{ij}^{md_2} \\ \vdots \\ \underline{\varphi}_{ij}^{md_D} \end{bmatrix}}_{\underline{\varphi}_{ij}} = \Omega \underbrace{\begin{bmatrix} (\underline{\phi}_i^{mm}, \ldots, \underline{\phi}_i^{md_D})^T \\ (\underline{\phi}_j^{mm}, \ldots, \underline{\phi}_j^{md_D})^T \end{bmatrix}}_{\underline{\phi}} \text{ where} \tag{10}$$

$$\Omega = \begin{bmatrix} -1 & 1 \end{bmatrix} \otimes I_{D+1}. \tag{11}$$

The concatenated vector $\underline{\phi}$ of dimension $2(D+1) \times 1$ results in a dispersion as

$$\underbrace{D\{\begin{bmatrix} (\underline{\phi}_i^{mm}, \ldots, \underline{\phi}_i^{md_D})^T \\ (\underline{\phi}_j^{mm}, \ldots, \underline{\phi}_j^{md_D})^T \end{bmatrix}\}}_{\underline{\phi}} = \underbrace{\begin{bmatrix} Q_{\phi_i} & Q_{\phi_i,\phi_j} \\ Q_{\phi_i,\phi_j} & Q_{\phi_j} \end{bmatrix}}_{Q_{\phi_{ij}}}, \tag{12}$$

where Q_{ϕ_i,ϕ_j} describes the covariance between the SD phases of point i and j. In Fig. 3 the third column illustrates $Q_{\phi_{ij}}$, of the concatenated vector $\underline{\phi}$. The difference between the clutter and the atmosphere component is discussed below in Sec. IV.

Subsequently, the VCM of the DD phases, $\underline{\varphi}_{ij}$, is computed with

$$Q_{\varphi_{ij}} = \Omega \; Q_{\phi_{ij}} \; \Omega, \tag{13}$$

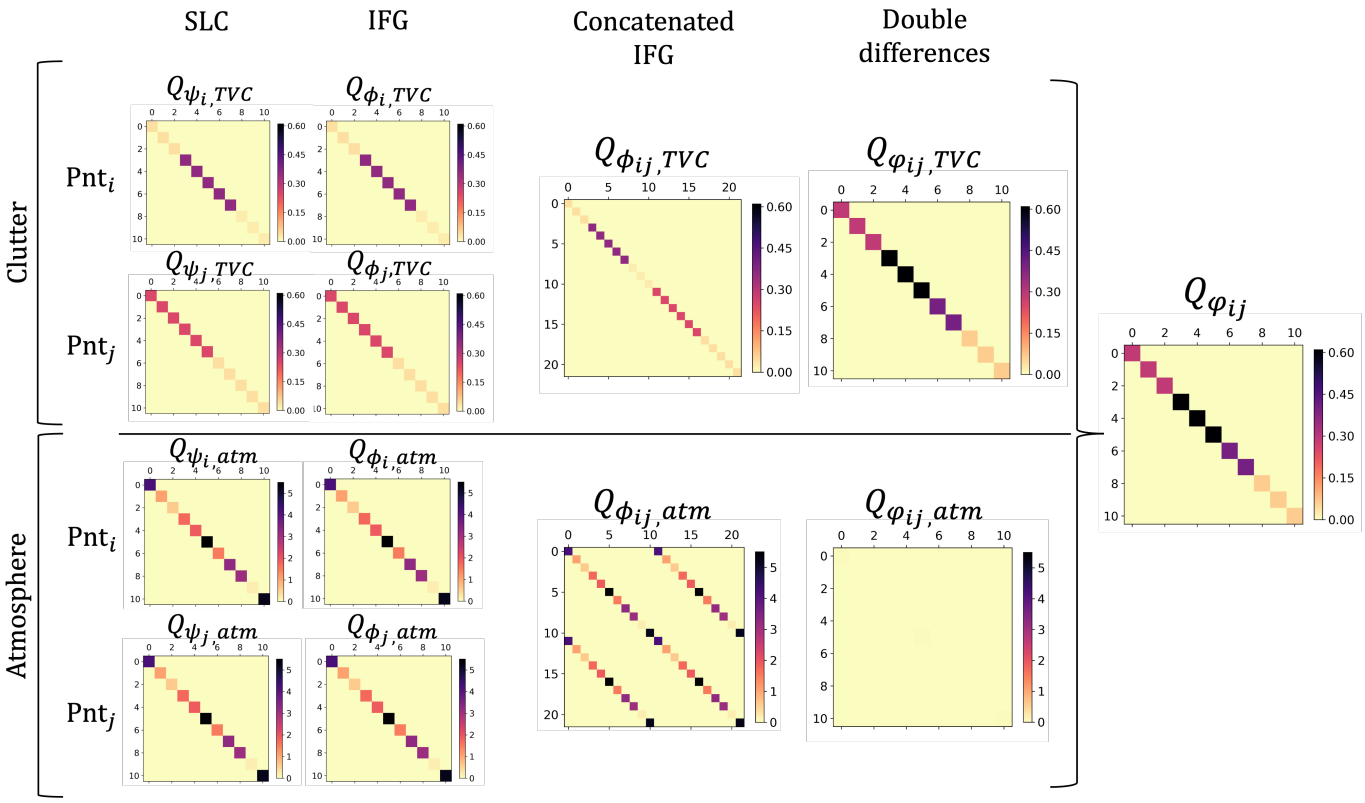

Fig. 3: An example of $Q_{\varphi_{ij}}$ as the sum of $Q_{\varphi_{ij},\text{TVC}}$ (above) and $Q_{\varphi_{ij},\text{atm}}$ below, for a *short* arc, i.e., $l \leq 200$ m. Column 1: VCM of the SLC phases of point i and j separately, with 11 epochs. For point i the time series was subdivided into three partitions, with one value $\sigma_{\psi,\text{TVC}}$ per partition, $\sigma_{\psi,\text{atm}}$ has a different value for every epoch. Column 2 shows that Q_{ϕ_i} and Q_{ϕ_j} are equal to Q_{ψ_i} and Q_{ψ_j} because of the deterministic nature of the mother SLC phase value that is subtracted to obtain the interferometric phases. Column 3 shows the VCM of the stacked interferometric phases of point i and j and the off diagonal part represents to correlation between the two points. Correlation in $Q_{\phi_{ij},\text{atm}}$ is observed because the simulated *short* arc. Consequently, column 4 represents $Q_{\varphi_{ij}}$ for the clutter and atmosphere separately, where it can be seen that it is still a diagonal matrix. Note that $Q_{\varphi_i,\text{atm}}$ is almost zero because of the high correlation between the two points. Finally, column 5 shows $Q_{\varphi_{ij}}$ that is the sum of $Q_{\varphi_{ij},\text{TVC}}$ and $Q_{\varphi_{ij},\text{atm}}$.

shown in the fourth, "Double differences", column of Fig. 3, with dimension $(D+1)\times(D+1)$. Thus, the dispersion of φ_{ij} depends on the dispersion of the SD values of both point i and point j, and the standard deviation of the DD phase $\sigma_{\varphi_{ij}^{md}}$ is

$$\sigma_{\varphi_{ij}^{md}} = \sqrt{\sigma^2_{\phi_i^{md}} + \sigma^2_{\phi_j^{md}}}, \tag{14}$$

in the case that there is no correlation between the two points. Below, in Sec. IV we show that for the TVC and the thermal noise this is a valid assumption.

In conclusion, we have shown that if the VCMs of the SLC phase observations are given, as well as the covariance between the two PS, the VCM of the DD interferometric phases can easily be derived. Below we address the method to obtain quantitative estimates of the relevant noise components.

IV. Noise component analysis

It follows from Eq. (3) that the VCM of the DD phase observations is defined as the sum of three components: i) the atmospheric noise, ii) the thermal noise, and iii) the time variant clutter. These will be discussed subsequently below.

A. Atmospheric noise

The troposphere causes a phase delay on the observed SLC phases, known as the Atmospheric Phase Screen (APS), depending on turbulent mixing and vertical stratification [1]. Since the turbulent atmospheric delay is completely uncorrelated between different acquisitions, all off-diagonal terms in $Q_{\psi_i,\text{atm}}$ are zero [1], and each individual epoch has a unique value. This is illustrated in the first column of Fig. 3 where we simulated $Q_{\psi,\text{atm}}$ for 11 epochs for two points.

While the APS is uncorrelated in time, it is spatially correlated, i.e., $Q_{\phi_i,\phi_j} \neq 0$, and depends on the distance between the two PS, typically following a power-law [1]. The single-epoch spatial covariance values can be approximated with

$$C_{\text{atm}}(l) = \sigma^2_{\text{atm}} \exp(-l^2\omega^2), \tag{15}$$

where l is the arc length (the distance between the two scatterers) and ω relates to the correlation length of the atmospheric signal l_c, and is defined as $\omega^2 = \ln(2)/l_c^2$. The lower block, "Atmosphere", of Fig. 3 shows the approximation of $Q_{\varphi_{ij},\text{atm}}$ for a *short* arc, i.e., $l \leq 200$ m. While the atmospheric phase delay for the SLC observations can be quite significant, the

variance of the atmospheric phase delay is close to zero for the DD phases for short arcs. This is because Q_{ϕ_i,ϕ_j}, which defines the correlation between the two scatterers, is almost equal to the variances of the SLC phase delays.[5]

B. Thermal noise

The thermal noise is caused by the radar instrument itself and is represented by the Noise Equivalent Sigma Zero (NESZ). For Sentinel-1 the NESZ has a value around -25 dB [16]. In Fig. 4 we show different realizations of the complex phasor for two PS. The observed phasor is always the sum of i) the signal, in this example constant over time and shown by the black phasor, ii) the clutter, shown in purple and blue, and iii) the thermal noise, shown in red. Since the thermal noise differs per epoch, the phasor will be different for every epoch.

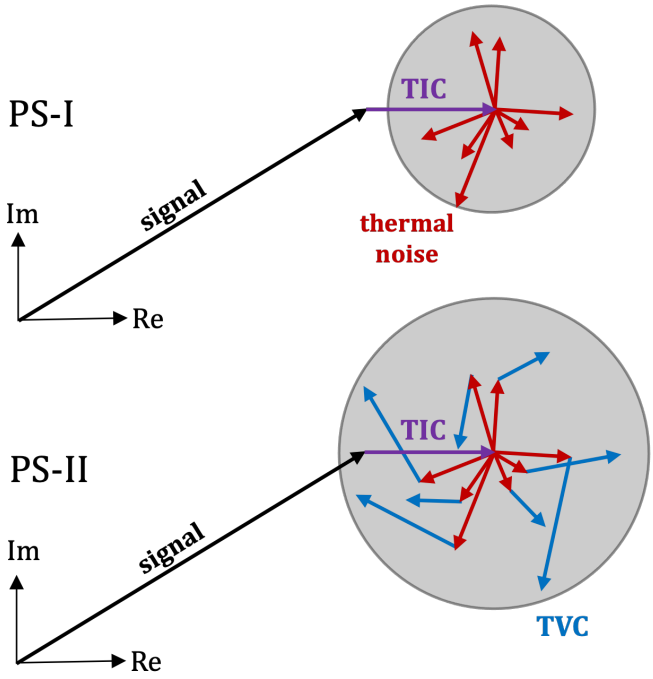

Fig. 4: Different realizations of the SLC phasor observations for two PS over time. The observed complex SLC phasor is the sum of four components. The signal, shown by the black phasor, and the Time Invariant Clutter, shown in purple, are both time invariant, i.e., the observations do not change over time. The thermal noise, shown by the red phasors, and the Time Variant Clutter, shown in blue, result in a different realization for each epoch. Therefore, also the summative combined phasor will have a different realisation over time. PS-I only has Time Invariant Clutter and thermal noise. The thermal noise expresses the noise on the final observation, as shown by the gray confidence circle behind it. PS-II also has some additional time variant clutter, resulting in a larger confidence circle.

[5]For long arc lengths, the influence of ionospheric delay needs to be included in Eq. (15), see [15]. For arcs between points with a significant height difference, the influence of stratification needs to be taken into account, see [1].

C. Time Variant Clutter

The observed SLC phase for one PS is the sum of all reflections within the same resolution cell. For ideal point scatterers there is often one dominant scatterer in the resolution cell. Thus, signals from other reflective objects within the same resolution cell can be regarded as noise, or clutter, as they are not necessarily related to the behavior of the main scatterer.

The clutter can be divided in two parts: the Time Invariant Clutter (TIC) and Time Variant Clutter (TVC). The TIC is the clutter that remains constant between different acquisitions. An extreme example would be a Corner Reflector (CR) on top of a rough concrete plate. The signal of interest is strong and relates to the CR, but the rough concrete surface also generates reflections that are considered clutter. When there is no displacement signal, the clutter caused by the concrete plate does not change over time, i.e., it is time *invariant*, see the purple TIC phasor in Fig. 4. Obviously, it is impossible to distinguish between the *signal* of interest and the TIC from the observations since both are time invariant. Consequently, both terms are combined into the signal phasor, and considered in the functional rather than the stochastic model.

On the contrary, the Time Variant Clutter (TVC) does change over time. An example would be a CR in a vegetated area. As long as the CR is not moving, the signal is constant, whereas the reflections caused by the vegetation differ per acquisition, see the blue phasors in Fig. 4. In the following we will first show how $Q_{\psi_i,\text{TVC}}$ can be derived and consequently how the values change over time.

1) The derivation of $Q_{\psi_i,\text{TVC}}$: The TVC and thermal noise both contribute to the noise in the SLC phase observations. However, from the complex SLC phase observations only it is not possible to distinguish between the two components. Therefore, the TVC and thermal noise will be lumped together in $Q_{\psi_i,\text{TVC}}$. Since both vary with time by definition, there is no correlation in time and $Q_{\psi_i,\text{TVC}}$ reduces to a diagonal matrix with variances values for the SLC phases on the diagonal, cf. Fig. 3, first column. From this point onward, we will discuss how $Q_{\psi_i,\text{TVC}}$ can be derived for PS. Note that the coherence matrix can be used to derive $Q_{\psi_i,\text{TVC}}$ for DS [17].

To estimate the phase contribution $\sigma_{\psi,\text{TVC}}$, also the magnitude of the signal itself is important. The effect of both noise components will be larger on low-magnitude PS compared to high-magnitude PS, i.e., the TVC concerns the ratio between the dominant point scatterer representing the signal and the rest of the reflecting objects in the resolution cell, and it is thus related to the SCR [18].

The Normalized Amplitude Dispersion (NAD) is a good proxy to estimate $\sigma_{\psi,\text{TVC}}$, with [4]

$$\sigma_{\psi,\text{TVC}} \approx \frac{\sigma_A}{\mu_A} = \text{NAD}, \tag{16}$$

where A is the vector of the amplitude time series, μ_A is its mean, and σ_A its standard deviation. However, the disadvantage of the NAD is that it is relatively sensitive to outliers, which are more likely in busy urban areas. This results in a rather pessimistic estimate of the phase quality, i.e., greater values for σ_A, the NAD, and consequently σ_ψ. As

a result, the outlier negatively affects the estimated quality of all observations.

To mitigate this effect, we introduce the Normalized Median Absolute Deviation (NMAD), defined by M_A, which is less affected by outliers, and is defined as

$$\mathrm{M}_A = \frac{\mathrm{MAD}}{\mathrm{med}(A)}, \tag{17}$$

where A is the vector representing the amplitude time series and $\mathrm{med}(A)$ the corresponding median. MAD is the Median Absolute Deviation that is defined as [19]

$$\mathrm{MAD} = \mathrm{med}(|A - \mathrm{med}(A)|). \tag{18}$$

Note that for normally distributed data the MAD is related to the standard deviation with

$$\sigma_A = k \cdot \mathrm{MAD}, \tag{19}$$

where $k \approx 1.4826$ [20]. Based on simulations as [8], [4], [21] we derive an empirical relation between the NMAD and $\sigma_{\psi,\mathrm{TVC}}$, see Fig. 5. We simulate phasors at various noise levels, using

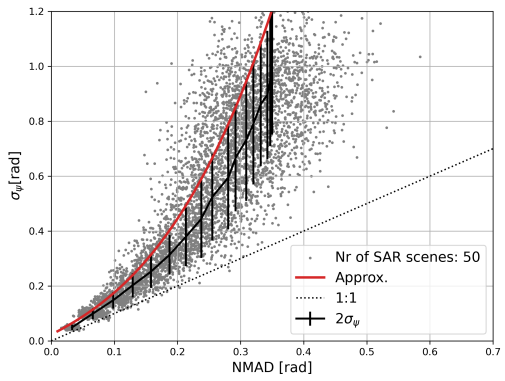

Fig. 5: We simulated scatterers for different noise levels consisting of 50 SAR scenes. For every scatterer (represented with a gray dot), we estimated the NMAD and σ_ψ. The black error bars represent the $2\sigma_\psi$ values that we computed per simulated noise level. The red line represents the derived empirical relation, see Eq.(20), between the NMAD and σ_ϕ based on the 2σ error bars. The dotted line represents the $1:1$ relation between the NMAD and σ_ϕ. Figure based on [4].

50 SAR scenes. For each phasor, both the NMAD and σ_ψ are computed and visualized as gray dots. For each noise level, the mean σ_ψ and its standard deviation are calculated and represented by 2σ black error bars. We then derive the relationship between NMAD and σ_ψ using the 97.7 percentile, i.e., $\mu+2\sigma$, shown by the red line. Using this percentile, instead of fitting through the mean of the cloud, we conservatively avoid overestimating the PS quality, acknowledging that real-world scenarios differ from simulations. In Sec. V-C we show the validity of this assumption with a test case on real data. The derived empirical relation is

$$\sigma_{\psi,\mathrm{TVC}} = 1.3\ \mathrm{M}_A + 1.9\ \mathrm{M}_A^2 + 11.6\ \mathrm{M}_A^3. \tag{20}$$

Hence, once we estimate M_A based on a given amplitude time series, we find an a priori estimate for the SLC phase quality.

2) Partitions: In reality, the amplitude of a scatterer may vary over time, and consequently so does $\sigma_{\psi,\mathrm{TVC}}$ [5]. Therefore, the time series can be subdivided into multiple partitions, where each partition has its own behavior. Four examples of this are shown in the upper row of Fig. 7. As long as there are enough observations within a partition, the M_A and consequently $\sigma_{\psi,\mathrm{TVC}}$ can be estimated. Since the amplitude behavior of scatterers may exhibit seasonal patterns, we chose the partitions to be not shorter than half a year.

As a result, for each partition of the time series the M_A and accordingly $\sigma_{\psi,\mathrm{TVC}}$ can be conservatively approximated with Eq. (20). All SLC phase observations within a partition have the same precision value of $\sigma_{\psi,\mathrm{TVC}}$, and these values are used to fill the diagonal of $Q_{\psi,\mathrm{TVC}}$, see Eq. (5). In Fig. 3 we show an example of the derivation of the VCM containing the sum of $Q_{\varphi_{ij},\mathrm{TVC}}$ (upper block) and $Q_{\varphi_{ij},\mathrm{atm}}$ (lower block). The first column of Fig. 3 shows this for two points (i and j) defining one arc with different partitions.

V. Results and Impact

The availability of a stochastic model of an arc that is independent on the actual displacement behavior is beneficial for the subsequent parameter estimation, the quality assessment of those parameters, and for testing the validity of the functional model. We test this for a descending Sentinel-1 time series over Amsterdam, detecting 1852 points across an area of approximately 700×800 m, see Fig. 6a. With this limited size we assume that the relative atmospheric delay is negligible, i.e., $Q_{\varphi,\mathrm{atm}} = 0$. For four example arcs, we show the derivation of $Q_{\varphi,\mathrm{TVC}}$, demonstrate the effect of incorporating $Q_{\varphi,\mathrm{TVC}}$ on the estimated parameters, and compare this to the case without a stochastic model. Then we show the effect of using a proper stochastic model on all the detected points.

A. Four example arcs

Fig. 7 shows the results of our method for the four different arcs shown in Fig. 6a. All four arcs share the same reference point, i, whose amplitude time series is shown in Fig. 6b, identifying four different partitions with NMAD values of 0.073, 0.060, 0.070, and 0.059 respectively, using a breakpoint detection method known as *ruptures* [22]. Using Eq. (20) this leads to the corresponding values for σ_{ψ_i}, i.e., 0.128, 0.105, 0.122 and 0.104 radians, respectively. The top row of Fig. 7 shows the amplitude time series for the four points P1–P4, each with distinct partitions. For example, in arc 1 (left column) three partitions were identified with NMAD values of 0.317, 0.0398, and 0.156, corresponding to σ_{ψ_j} values of 0.985, 1.561, and 0.31 radians. Consequently, arc 1 of P1 with reference point i, which had four partitions, has a total of six partitions, and thus six distinct values for $\sigma_{\phi_{ij}}$.

The second row of Fig. 7 shows the resulting $Q_{\varphi,\mathrm{TVC}}$, which is a diagonal matrix, cf. Fig. 3. The horizontal blue lines are an alternative representation of the diagonal values of $Q_{\varphi_{ij}}$ (refer to the right axis). The six values of $\sigma_{\varphi_{ij}}$ are 0.944, 1.566, 1.564, 1.565, 0.333, and 0.326 radians, indicating that

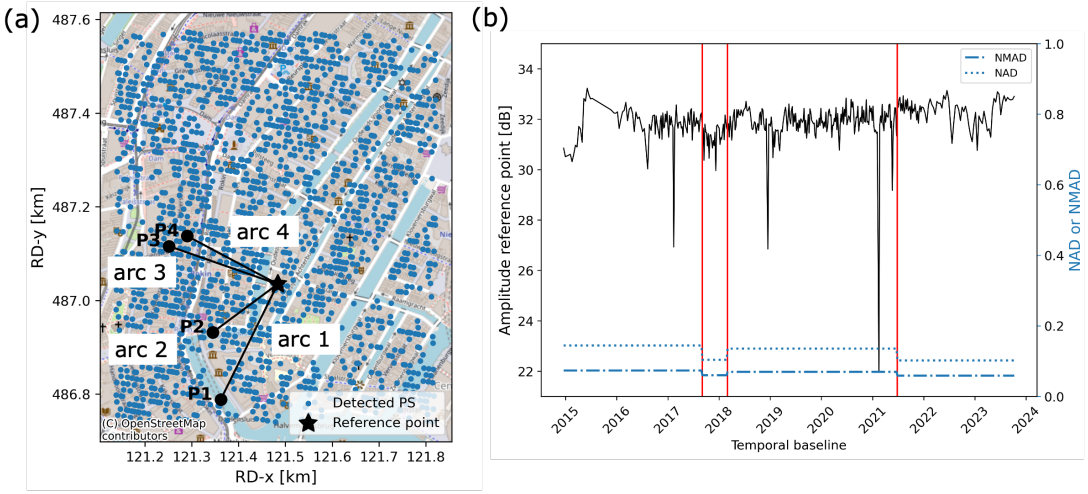

Fig. 6: **A)** Detected PS over Amsterdam and the four example arcs that are highlighted in Fig. 7. **B)** Amplitude time series for the reference point. Four different partitions are detected using a breakpoint detection algorithm. For each partition, the NAD and NMAD are calculated. Using the NMAD values and Eq. (20) we estimate the standard deviation of the SLC phase values that fall within that partitions.

the quality of the last two partitions is significantly better than that of the first four. This interpretation is supported by the double-difference phase observations for the arc, shown in the third row of Fig. 7. The black and gray dots represent the observed double-difference phases and the corresponding 2π-ambiguity levels, respectively. As expected, the dispersion of the DD phases within the first four partitions (up to March 2019) is greater than in the later observations.

The proposed stochastic model is now used to estimate the unknown parameters, i.e., a linear velocity D_A, thermal component $\mu_{\Delta T} L_{\text{LoS}}$ (where $\mu_{\Delta T}$ is the linear expansion coefficient and L_{LoS} is the dimension of the object in the LoS direction), and relative residual cross range distance H_{ij}, as shown in Eq. (2). We estimate these three unknown parameters using

$$\underline{\hat{x}} = Q_{\hat{x}} A^T Q_y^{-1} \underline{y}, \text{ with} \tag{21}$$

$$Q_{\hat{x}} = (A^T Q_y^{-1} A)^{-1}, \tag{22}$$

where $Q_{\hat{x}}$ is the variance-covariance matrix of the estimates of the unknown parameters $\underline{\hat{x}}$. Here, $\underline{y}$ are the double difference phase observations of the arc. To evaluate the performance of the parameter estimation, we compare the newly developed stochastic model, $Q_{\varphi_{ij}}$, with a unit weight matrix Q_{UW}, which would be equivalent to a conventional result. The estimated parameters are shown in Table I.

Additionally, we compute the double-difference absolute phase using the estimated parameters, i.e., $\hat{\varphi}_{ij} = A\underline{\hat{x}}$, with results for both $Q_{\varphi_{ij}}$ (weighted) and Q_{UW} (unweighted) represented by the blue and red lines, respectively, in the third row of Fig. 7[6]. For arc 1, we estimate a linear velocity of 0.7 mm/y using the weighted matrix, where the first noisier observations were assigned lower weights. In contrast, the estimated linear velocity using the unweighted matrix was 1.4 mm/y, a significant difference. While the differences between the red and blue lines in the third row of Fig. 7 may appear negligible, the effect of a proper weight matrix will be more influential with a shorter time series.

We also compute the residuals between the observations and the evaluated model, i.e., $\underline{\hat{e}} = \underline{\varphi}_{ij} - \underline{\hat{\varphi}}_{ij}$, shown in the bottom row of Fig. 7. We visualize the 95% confidence interval based on the computed $Q_{\varphi_{ij}}$ with the blue horizontal lines, which shows that the confidence interval for the first partitions is indeed bigger than for the observations in the other three partitions. Clearly, when both the functional and stochastic model are correct, 95% of the residues (black dots) should lie within the 95% confidence bounds based on the diagonal of $Q_{\varphi_{ij}}$. The same behavior can be observed for the other three arcs, suggesting that using partitions for $Q_{\varphi_{ij}}$ is valuable for quality assessment and parameter estimation. The proposed stochastic model is defined *prior* to parameter estimation—a key difference from conventional methods, where quality of scatterers is only determined retrospectively by analyzing the residuals between the model and observations. This distinction is illustrated by the red line in the bottom row of Fig. 7. The advantage of the proposed stochastic model is obvious: assessing observation quality only in hindsight fails to account for variations over time. For instance, in arc 1, the red line shows that quality is overestimated in the first half of the time series and underestimated in the second half. Furthermore, conventional methods rely heavily on accurate parameterization (i.e., a correct functional model), and consequently unmodeled displacements are attributed to the stochastic model. This can be particularly problematic in the built environment, where many different displacement signals may be present.

B. Results over Amsterdam

To demonstrate that the stochastic model indeed results in different estimated parameters, and that the examples shown

[6]The unit weight matrix was calculated using the mean value of the diagonal of $Q_{\varphi_{ij}}$

TABLE I: Properties and estimated parameters for the four arcs shown in Fig. 7. The W and UW between brackets indicate a weighted or unweighted estimation respectively. The $\pm$ margins indicate 2σ values. All parameters estimated using the proposed stochastic model exhibit less uncertainty.

		Arc 1	Arc 2	Arc 3	Arc 4
Arc length	[m]	274.96	172.76	245.60	219.15
Average sigma	[rad]	0.83	0.42	0.67	0.94
Cross range (W)	[m]	13.69 ± 1.54	-8.09 ± 1.25	12.73 ± 1.81	-7.66 ± 1.80
Cross range (UW)	[m]	19.77 ± 3.03	-5.47 ± 1.64	15.53 ± 2.92	-6.37 ± 3.02
Thermal (W)	[mm/K]	0.11 ± 0.02	-0.11 ± 0.01	0.08 ± 0.02	-0.02 ± 0.02
Thermal (UW)	[mm/K]	-0.08 ± 0.03	-0.12 ± 0.02	0.09 ± 0.03	-0.02 ± 0.03
Velocity (W)	[mm/yr]	-0.69 ± 0.06	-0.02 ± 0.04	0.78 ± 0.05	-0.97 ± 0.08
Velocity (UW)	[mm/yr]	-1.38 ± 0.09	-0.15 ± 0.05	0.34 ± 0.08	-0.77 ± 0.09

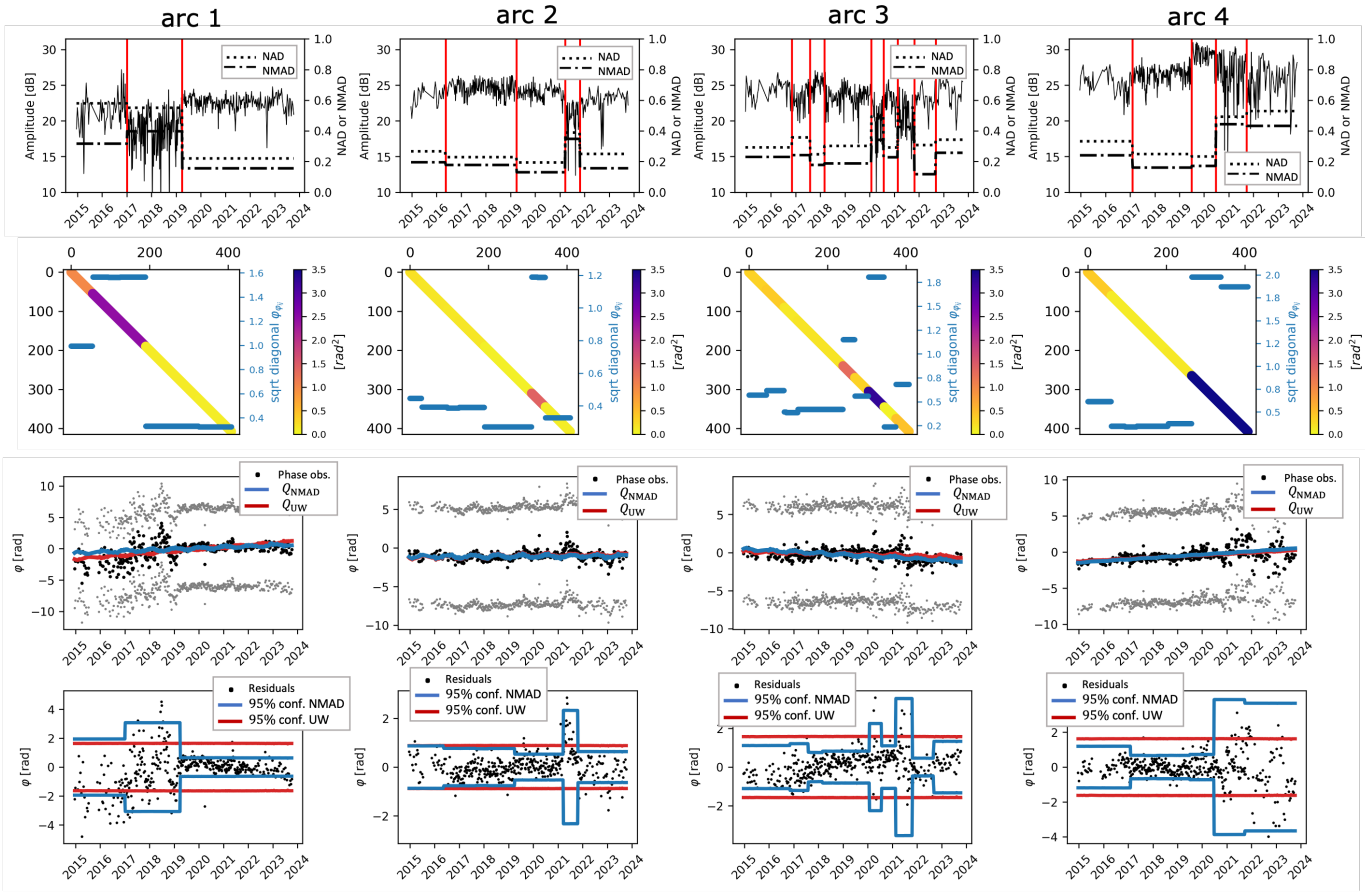

Fig. 7: Four example arcs. The top row shows the amplitude time series, together with the detected partitions indicated by the red vertical lines, for points 1 to 4 of Fig. 6a. The horizontal dotted and dash-dotted lines represent the NAD and NMAD values per partitions, respectively, indicated on the vertical axis on the right side. The second row shows the VCM, $Q_{\varphi_{ij}}$, for the arc with the colorbar corresponding to the values in the matrix. The observations are uncorrelated, i.e., the off-diagonal elements are zero. The horizontal blue lines correspond to the square root of the diagonal of $Q_{\varphi_{ij}}$, and the values are shown on the vertical axis on the right side (in blue). These values clearly differ per partition. The third row shows the double-difference phase observations for the arc and the proposed stochastic model using $Q_{\varphi_{ij}}$, corresponding to the blue line, and using a unit-weight matrix, corresponding to the red line. Especially for arc 1, using a different variance-covariance matrix results in different estimated model parameters. The last row shows the residues between the estimated model and the observations shown by the black dots, and confidence intervals using the $Q_{\varphi_{ij}}$ and the unit weight matrix (UW, unweighted). Using the proposed method for the variance-covariance matrix makes sense, since we indeed find larger residues for the partitions that are assigned a lower quality.

in Fig. 7 are not anecdotal, we estimate the linear velocity, relative residual cross range distance, and thermal component for all points. In Fig. 8 we show the histograms of the differences between the estimates using the two weight matrices. Differences in linear velocity can be up to 1 mm/y, and relative cross range distance up to ± 7 m. While the differences cannot be used to uniquely identify the 'correct' solution, it is clear that the stochastic model contributes more (independent) information to the inverse problem, making it at least more likely that including $Q_{\varphi_{ij}}$ leads to more reasonable parameter estimates.

C. Comparison a priori and posteriori sigma values

If the a priori stochastic model $Q_{\varphi_{ij}}$ indeed represents the noise of that particular arc, and the functional model used to estimate the unknown parameters represents its behavior, then the priori sigma ($Q_{\varphi_{ij}}$) should approximate the posterior sigma, i.e., it would match the standard deviation of the residuals between the observed DD and the estimated DD values. Here we validate the proposed stochastic model, assess whether indeed the NMAD is preferred over the NAD, and confirm whether the derived relation between the NMAD and σ_ψ as in Eq. (20) is valid.

To this end, we estimate the unknown parameters for all points shown in Fig. 6a using three different stochastic models. The first stochastic model is the proposed one, using the NMAD per partition, and Eq. (20) for the relation between the NMAD and σ_ψ using the 97.7 percentile. The second model also relies on NMAD values per partition but uses the 50th percentile, as represented by the black line in Fig. 5. The third model uses the NAD per partition instead of NMAD, with a similar relationship between NAD and σ_ψ derived from the 97.7 percentile.

We estimate the unknown parameters per point using the three different stochastic models. Consequently, the posterior sigma values were estimated, and we computed the correlation between the assumed a priori sigma and the calculated posterior sigmas. If our stochastic model would be perfect, we expect a correlation of 1. The results are 0.48, 0.46, and 0.15 for model 1, model 2, and model 3, respectively.[7] These results show that the NMAD is preferred over the NAD since both models 1 and 2 result in a correlation that is $\sim$3 times greater than model 3. Moreover, the relation that is based on using the 97.7 percentile values from the simulation results in a slightly higher correlation compared to the 50th percentile. The reason why the correlation values are not closer to 1 is to be explained by the partitions. The partitions as detected for a single point consist of at least 30 observations. However, the stochastic model for an arc is based on the partitions of both point i and point j. Thus it is feasible that we evaluate arc partitions that contain less then 30 observations, for which it is difficult to compute statistics as the posterior sigma.

VI. Conclusion

The fundamental problem of parameter estimation from InSAR time series is that both the functional models and the stochastic model are unknown and different for each scatterer and epoch. Conventionally, the same functional model is chosen for all points in the area of interest, and the quality of an arc is assessed retrospectively by analyzing residuals between the observations and the model, creating a strong and undesired dependency on the accuracy of the functional model. A stochastic model for double-difference phase observations of an arc is proposed, independent of the functional model, defined *prior* to parameter estimation. It is shown how the reference (mother) acquisition needs to be handled in the estimation procedure to obtain a diagonal VCM for the temporal single-differences, which is numerically beneficial. Using the amplitude vector per point, subdivided in temporal partitions, and its Normalized Median Absolute Deviation (NMAD), which is less sensitive to outliers than the conventional NAD, the variance-covariance matrix of the double differences of the arc is derived.

The result is an independent a priori stochastic model for each individual point (and arc) in the area of interest, describing time variable quality values of the observations.

This allows us to discriminate between points based on expected quality, between relevant epochs, and assign different weights to observations from different time periods. Incorporating these weights improves the estimation of unknown parameters, making it a critical component of the parameter estimation process.

[7]Note that we compared the prior and posterior sigmas per partition, since sigma values do not vary within one partition.

Acknowledgment

This research is part of the DeepNL project, and is supported by the Dutch Research Council (NWO), grant no.: DEEPNL.2018.052.

References

[1] R. F. Hanssen, *Radar Interferometry: Data Interpretation and Error Analysis*. Dordrecht: Kluwer Academic Publishers, 2001.

[2] ——, "Stochastic modeling of time series radar interferometry," in *IGARSS 2004. 2004 IEEE International Geoscience and Remote Sensing Symposium*, vol. 4. IEEE, 2004, pp. 2607–2610.

[3] K.-R. Koch, *Parameter estimation and hypothesis testing in linear models*. Berlin: Springer-Verlag, 1999.

[4] A. Ferretti, C. Prati, and F. Rocca, "Permanent scatterers in SAR interferometry," *IEEE Transactions on Geoscience and Remote Sensing*, vol. 39, no. 1, pp. 8–20, Jan. 2001.

[5] F. Hu, J. Wu, L. Chang, and R. F. Hanssen, "Incorporating temporary coherent scatterers in multi-temporal InSAR using adaptive temporal subsets," *IEEE transactions on geoscience and remote sensing*, vol. 57, no. 10, pp. 7658–7670, 2019.

[6] B. Van De Kerkhof, V. Pankratius, L. Chang, R. Van Swol, and R. Hanssen, "Individual scatterer model learning for satellite interferometry," *IEEE transactions on geoscience and remote sensing*, vol. 58, no. 2, pp. 1273–1280, 2019.

[7] F. Hu and J. Wu, "Detecting spatio-temporal urban surface changes using identified temporary coherent scatterers," *Journal of Systems Engineering and Electronics*, vol. 32, no. 6, pp. 1304–1317, 2021.

[8] F. J. van Leijen, "Persistent scatterer interferometry based on geodetic estimation theory," Ph.D. dissertation, Delft University of Technology, Delft, the Netherlands, 2014.

[9] L. Chang and R. F. Hanssen, "A probabilistic approach for InSAR time-series postprocessing," *IEEE transactions on geoscience and remote sensing*, vol. 54, no. 1, pp. 421–430, 2016.

[10] A. Hooper, H. Zebker, P. Segall, and B. Kampes, "A new method for measuring deformation on volcanoes and other non-urban areas using InSAR persistent scatterers," *Geophysical Research Letters*, vol. 31, pp. L23 611, doi:10.1029/2004GL021 737, Dec. 2004.

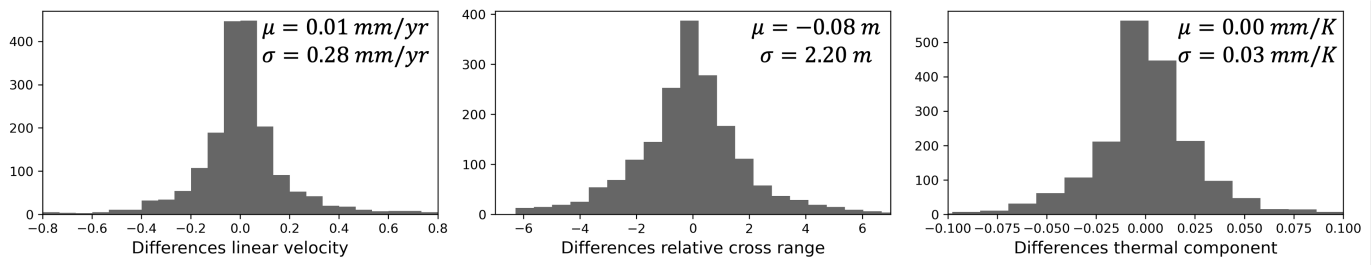

Fig. 8: For all points shown in Fig. 6a we estimated the linear velocity, relative residual cross range distance, and thermal component using two weight matrices: i) with our method and ii) the unit weight matrix. The differences between the estimated parameters are shown in the histograms.

[11] F. Vecchioli, M. Costantini, F. Minati, and M. Zavagli, "A novel algorithm for point coherence estimation in SAR Interferometry," in *IGARSS 2023-2023 IEEE International Geoscience and Remote Sensing Symposium*. IEEE, 2023, pp. 7868–7871.

[12] Z. Yunjun, H. Fattahi, and F. Amelung, "Small baseline InSAR time series analysis: Unwrapping error correction and noise reduction," *Computers & Geosciences*, vol. 133, p. 104331, 2019.

[13] W. S. Brouwer, Y. Wang, F. van Leijen, and R. F. Hanssen, "On the stochastic model for InSAR single arc point scatterer time series," in *IGARSS 2023-2023 IEEE International Geoscience and Remote Sensing Symposium*. IEEE, 2023, pp. 7902–7905.

[14] A. Ferretti, C. Prati, and F. Rocca, "Nonlinear subsidence rate estimation using permanent scatterers in differential SAR interferometry," *IEEE Transactions on geoscience and remote sensing*, vol. 38, no. 5, pp. 2202–2212, 2000.

[15] M. Eineder, C. Minet, P. Steigenberger, X. Cong, and T. Fritz, "Imaging geodesy – toward centimeter-level ranging accuracy with TerraSAR-X," *Geoscience and Remote Sensing, IEEE Transactions on*, vol. 49, no. 2, pp. 661–671, 2011.

[16] R. Torres, I. Navas-Traver, D. Bibby, S. Lokas, P. Snoeij, B. Rommen, S. Osborne, F. Ceba-Vega, P. Potin, and D. Geudtner, "Sentinel-1 SAR system and mission," in *2017 IEEE Radar Conference (RadarConf)*. IEEE, 2017, pp. 1582–1585.

[17] S. S. Esfahany, "Exploitation of distributed scatterers in synthetic aperture radar interferometry," Ph.D. dissertation, Delft University of Technology, Delft, the Netherlands, 2017.

[18] P. Shanker and H. Zebker, "Persistent scatterer selection using maximum likelihood estimation," *Geophysical Research Letters*, vol. 34, no. 22, 2007.

[19] C. Leys, C. Ley, O. Klein, P. Bernard, and L. Licata, "Detecting outliers: Do not use standard deviation around the mean, use absolute deviation around the median," *Journal of experimental social psychology*, vol. 49, no. 4, pp. 764–766, 2013.

[20] P. J. Rousseeuw and C. Croux, "Alternatives to the median absolute deviation," *Journal of the American Statistical association*, vol. 88, no. 424, pp. 1273–1283, 1993.

[21] B. M. Kampes, "Displacement parameter estimation using permanent scatterer interferometry," Ph.D. dissertation, Delft University of Technology, Delft, the Netherlands, 2005.

[22] C. Truong, L. Oudre, and N. Vayatis, "Selective review of offline change point detection methods," *Signal Processing*, vol. 167, p. 107299, 2020.

Wietske Brouwer received the BSc degree and MSc degrees in Civil Engineering from Delft University of Technology in 2018 and 2021, respectively. She is currently pursuing her PhD degree at TU Delft, working on mathematical aspects of satellite radar interferometry.

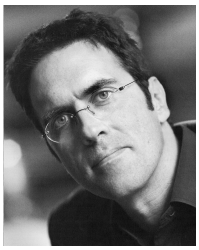

Ramon F. Hanssen (M'04-SM'15) received the M.Sc. degree in Geodetic Engineering and the Ph.D. degree (cum laude) from Delft University of Technology, The Netherlands, in 1993 and 2001, respectively.

He was with the International Institute for Aerospace Survey and Earth Science (ITC), Stuttgart University, Stuttgart, Germany; the German Aerospace Center (DLR), Weßling, Germany; Stanford University, Stanford, CA, USA, as a Fulbright Fellow; and the Scripps Institution of Oceanography, University of California at San Diego, La Jolla, CA, USA, involved in microwave remote sensing, radar interferometry, signal processing, and geophysical application development. Since 2008, he has been an Antoni van Leeuwenhoek Professor in earth observation with the Delft University of Technology, where he has been leading the research group on mathematical geodesy and positioning since 2009. He has authored a textbook on radar interferometry.